Direct Observations of Austenite, Bainite, and Martensite Formation during Arc Welding of 1045 Steel Using Time-Resolved X-ray Diffraction

Phase transformations were tracked in real time using a synchrotron accelerator

BY J. W. ELMER, T. A. PALMER, S. S. BABU, W. ZHANG, AND T. DeBROY

ABSTRACT. In-situ time-resolved X-ray diffraction (TRXRD) experiments were performed during stationary gas tungsten arc (GTA) welding of AISI 1045 C-Mn steel. These real-time synchrotron-based experiments tracked phase transformations in the heat-affected zone of the weld under rapid heating and cooling conditions. The diffraction patterns were recorded at 100 ms intervals, and were later analyzed using diffraction peak profile analysis to determine the relative fraction of ferrite (α) and austenite (γ) phases in each diffraction pattern. Lattice parameters and diffraction peak widths were also measured throughout the heating and cooling cycle of the weld, providing additional information about the phases that were formed. The experimental results were coupled with temperatures calculated by a thermo-fluids weld model, allowing the transformation kinetics of the $\alpha\rightarrow\gamma$ phase transformation to be evaluated. During heating, complete austenitization was observed in the heat-affected zone of the weld, and the kinetics of the $\alpha\rightarrow\gamma$ phase transformation were modeled using a Johnson-Mehl-Avrami (JMA) approach. The results from the 1045 steel weld were compared to those of a 1005 low-carbon steel from a previous study. Differences in austenitization rates of the two steels were attributed to differences in the base metal microstructures, particularly the relative amounts of pearlite and the extent of the allotriomorphic ferrite phase. During weld cooling, the austenite transformed to a mixture of bainite and martensite. In situ diffraction was able to distinguish between these two nonequilib-

rium phases based on differences in their lattice parameters, diffraction peak widths, and their transformation rates, resulting in the first real-time X-ray diffraction observations of bainite and martensite formation made during welding.

Introduction

Transformations between the body-centered cubic (BCC) form of iron (α-ferrite) and the face-centered cubic (FCC) form of iron (γ-austenite) during heating and cooling are principally responsible for the microstructure and properties of steels. These transformations have been studied in great detail for many decades to establish optimum thermal-mechanical processing treatments for a wide variety of steels (Refs. 1–3). However, when steels are welded, the optimized base metal properties are altered by the localized weld thermal cycles. The result is the creation of nonequilibrium microstructures in the weld fusion zone (FZ) and heat-affected zone (HAZ). These microstructures are significantly different in both appearance and properties from those found in the base metal (Refs. 4–6). Such nonequilibrium phases can compromise the integrity of the weld joint, making it important to understand how the welding conditions lead to their creation.

In widely used C-Mn steels, the carbon content of the steel plays an important role in the microstructural evolution of the weld. As the carbon content increases, welding-induced changes in the microstructure become more pronounced due to the nonuniform distribution of carbon in the microstructure. These changes are most prominent during the rapid weld cooling, which further intensifies these effects, resulting in microstructures that deviate significantly from equilibrium. The mechanisms responsible for these transformations are well known (Refs. 4–6); however, few direct observations of the transformation sequence have been reported.

Previous investigations of low-carbon steel containing 0.05 wt-% C served as a baseline for the experiments on the medium-carbon 1045 steel presented here. The earlier work on low-carbon steel was performed in situ using synchrotron radiation under both spatially resolved (Refs. 7, 8) and time-resolved experimental conditions (Ref. 9). Kinetic parameters were determined, allowing the prediction of the $\alpha\rightarrow\gamma$ transformation during weld heating of the low-carbon steel to be made (Ref. 8). In this investigation, a medium-carbon steel containing 0.46 wt-% carbon was rapidly heated and cooled during stationary arc welding. During welding, synchrotron radiation was also used to track the phase transformations that occurred in the HAZ of the weld. These experiments produced a series of X-ray diffraction patterns revealing the real-time crystal structure of the weld. Results of these observations showed complete austenitization of the initial microstructure during rapid weld heating, and subsequent transformations during rapid weld cooling. Quantitative information about the phase transformation kinetics was extracted from these data through thermal and phase transformation modeling. These results were compared to those of the low-

J. W. ELMER and T. A. PALMER are with the Lawrence Livermore National Laboratory, Livermore, Calif. S. S. BABU is with the Oak Ridge National Laboratory, Oak Ridge, Tenn., W. ZHANG and T. DeBROY are with Pennsylvania State University, University Park, Pa.
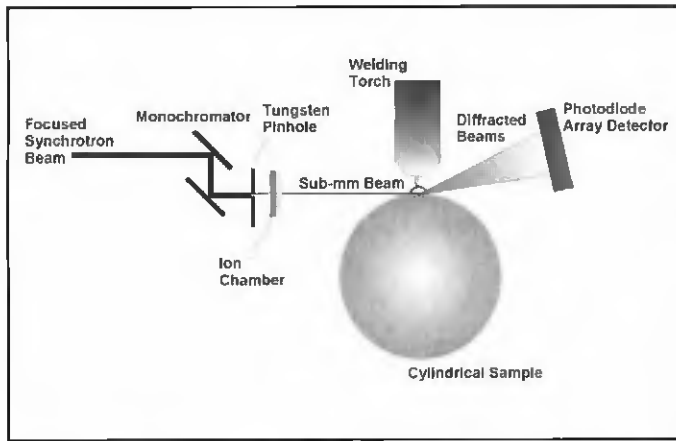

KEY WORDS

Time-Resolved X-ray Diffraction
Synchrotron Radiation
Phase Transformations
Kinetics
Austenite
Bainite
Martensite
Arc Welding
Steels
Heat-Affected Zone

Fig. 1 — Schematic diagram of the TRXRD experimental setup for synchrotron-based in situ observations of phase transformations during welding.
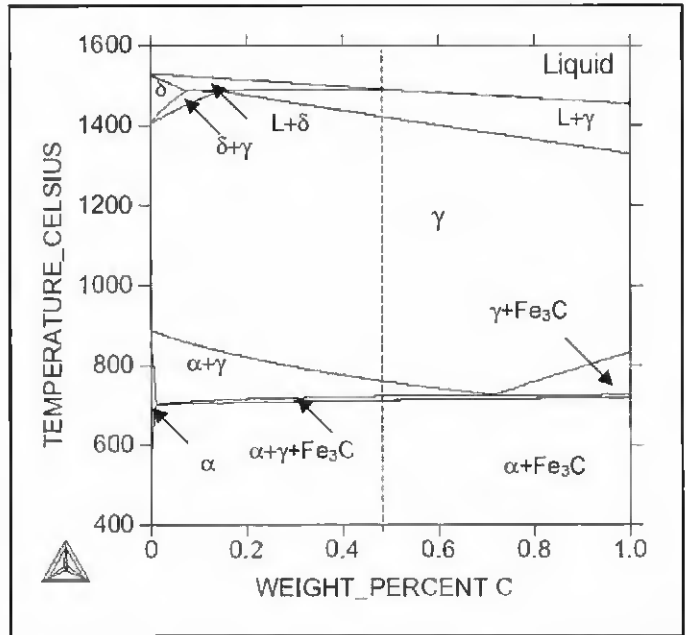

Fig. 2 — Calculated pseudo-binary phase diagram for the AISI 1045 steel. The nominal carbon concentration of the alloy is indicated as the vertical dashed line.

carbon steel to better understand the influence of carbon content on phase transformations that occur during the welding of steel.

Differences in the phase transformation behavior of the low- and medium-carbon steels were apparent. During heating, the kinetics of the α→γ transformation showed that the 1045 steel initially transformed at a higher rate than the 1005 steel but then slowed down, eventually requiring more time to transform than the 1005 steel. This difference was associated with differences in the starting microstructures of the two steels. During cooling, the high rates produced during the stationary arc spot welding technique used in the TRXRD experiments proved to be rapid enough to produce a combination of bainite (nonlamellar ferrite plus Fe$_3$C) and martensite (interstitial carbon) in the microstructure of the 1045 steel, but these phases were not observed in similar experiments on the low-carbon steels.

The results presented here demonstrate not only differences in the phase transformation behavior between low- and medium-carbon steels, but also how in-situ X-ray diffraction can be used to provide real-time observations of important phase transformations during the welding of steels.

Experimental Procedures

TRXRD Experiments

Gas tungsten arc (GTA) welds were made on AISI 1045 forged steel bars having the following composition: (0.46 C, 0.85 Mn, 0.27 Si, 0.02 Ni, 0.11 Cr, 0.014 P, 0.01 Cu, 0.02 S, 0.027 Al, 0.001 Nb, 0.01 Mo, 0.005 V; by wt-%). These samples were machined from 10.8-cm-diameter forged bar stock into welding samples, 12.7 cm long and 10.2 cm diameter. Welds were then made on the cylindrical steel

bars in an environmentally sealed chamber to avoid atmospheric contamination of the welds. A schematic illustration of the experimental setup is shown in Fig. 1, and a brief summary of the welding parameters used here is given in Table 1. Further details of similar welding experiments have been previously reported for titanium and titanium alloys (Refs. 10, 11), other steels (Ref. 12), and stainless steel alloys (Refs. 13, 14).

The in situ TRXRD experiments were performed during welding using the 31-pole wiggler beam line, BL 10-2, at Stanford Synchrotron Radiation Laboratory (SSRL) with SPEAR (Stanford Positron-Electron Accumulation Ring) operating at an electron energy of 3.0 GeV and an injection current of ~100 mA. As illustrated in Fig. 1, a focused monochromatic synchrotron X-ray beam was passed through a 540-mm tungsten pinhole to render a submillimeter beam on the sample at an incident angle of ~25 deg. This setup yielded a beam flux on the sample of ~10^{12} photons/s, which was determined experimentally using an ion chamber immediately downstream from the pinhole. A photon energy of 12.0 keV ($\lambda = 0.1033$ nm) was chosen to facilitate phase identification and to be far enough in energy above the Fe K-edge (7.112 keV) to minimize the background contribution due to Fe K-fluorescence from the steel sample.

X-ray diffraction patterns were recorded using a 50-mm-long 2048-element position-sensitive Si photodiode array detector. The array was mounted on a dual-stage water-cooled Peltier-effect thermoelectric cooler at a distance of approximately 10 cm behind the weld to cover a 2θ range from 22 to 52 deg. This

Table 1 — Summary of GTA Welding Parameters Used in the TRXRD Experiments

Welding electrode	W (2% Th)
Electrode diameter	4.7 mm
Torch polarity	DCEN
Maximum current	175 A
Background current	131 A
Pulsing frequency	300 Hz
Peak on time	50%
Shielding gas	helium
Arc on time	17 s
Resulting fusion zone width	9.9 ± 0.66 mm

2θ range was optimized to contain a total of six diffraction peaks, three from the BCC phase (α-Fe) and three from the FCC phase (γ-Fe). Calibration of the X-ray diffraction patterns was performed using a thin niobium foil, which has a well-characterized BCC crystal structure.

Analysis of each peak in every diffraction pattern was performed to determine the semiquantitative volume fractions of ferrite and austenite present as a function of welding time. This analysis measured the integrated intensity of each peak using a sum of one or more Gaussian peak profile-fitting functions using an automated curve-fitting routine developed in *Igor Pro®, Version 4.0* (Ref. 14). The raw integrated intensities of the diffraction peaks were then converted into phase fractions by dividing the integrated peak area for
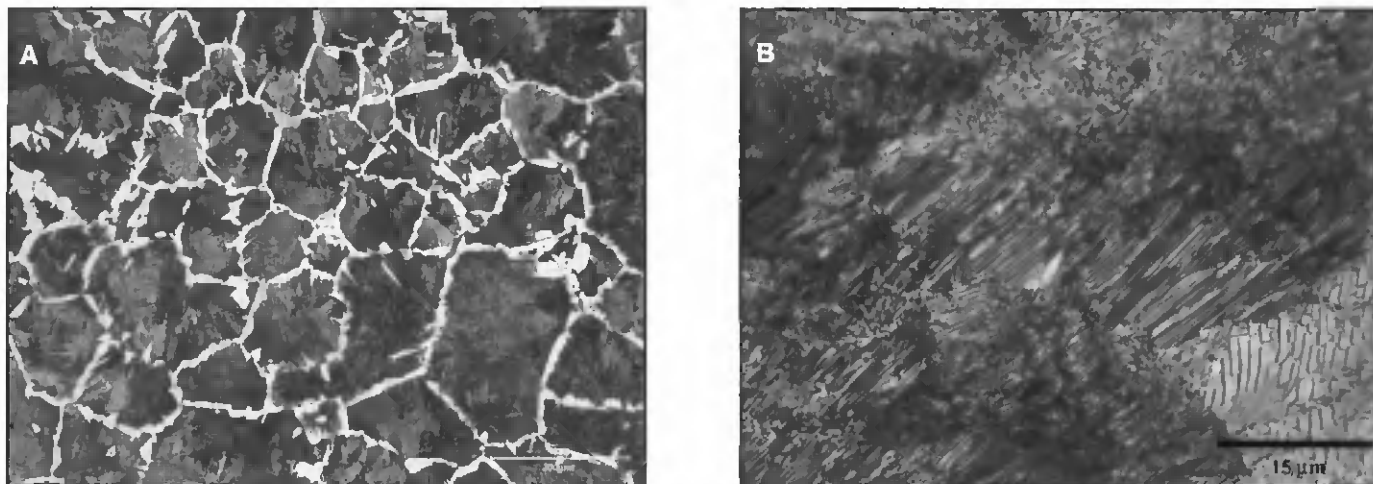
Fig. 3 — A — Base metal microstructure showing allotriomorphic ferrite outlining the prior austenite grains and pearlite colonies inside the grains. B — high-magnification optical micrograph showing the lamellar microstructure typical of the pearlite colonies within the grains.

the BCC phase by the total integrated areas of the BCC and FCC phases. The fraction of the FCC phase was then determined as the difference between unity and the BCC fraction, since only two phases were observed in this system.

Phase Equilibria and Base Metal Microstructure

The phase transformation sequence in the 1045 steel was calculated from thermodynamic relationships using *Thermocalc* and the *Fe2000* database (Ref. 15). These calculations were used to determine the transformation temperatures for the AISI 1045 steel by considering the effects of Fe, C, Si, Mn, Ni, and Cr on the liquid, ferrite, austenite, and cementite phase fields. The calculated phase-boundary temperatures for this multicomponent alloy are illustrated in the pseudo-binary diagram shown in Fig. 2. In this figure, the vertical dashed line indicates the nominal carbon content of the alloy.

The thermodynamic calculations indicate that the equilibrium starting microstructure of this alloy consists of a mixture of ferrite and Fe_3C carbide phases. During heating, this microstructure begins to transform to austenite when the A1 temperature of 712°C is reached. Complete transformation to austenite occurs when the A3 temperature of 765°C is reached, and this austenite remains stable until melting begins to occur at 1410°C. These transformations reverse during cooling; however, kinetic limitations may alter the predicted phase transformation start and completion temperatures, and may produce nonequilibrium phases.

The starting microstructure of the 1045 steel is shown in Fig. 3A as revealed by polishing the base metal and etching in a 2% nital (nitric acid and alcohol) solution.

This microstructure contains allotriomorphic ferrite, which is the light etching phase that outlines the prior austenite grain boundaries. Inside the prior austenite grains, the microstructure consists of pearlitic colonies, which etch dark and occupy the majority of the microstructure. A higher magnification micrograph highlighting the lamellar structure of the pearlite is shown in Fig. 3B. Quantitative metallography was performed on this microstructure using *Image Pro*, *Version 4.1*. Measurements of the area fraction of allotriomorphic ferrite made at several locations indicate that the microstructure contains 12% allotriomorphic ferrite and 88% pearlite. The prior austenite grain size of the base metal was measured to be 92.8 µm in diameter. In addition, the size of the allotriomorphic grain boundary ferrite phase was shown to be 15 to 20 µm wide on average, with some patches reaching 30 µm or more in places.

Coupled Thermal-Fluids Numerical Modeling of Weld Temperatures

The TRXRD experimental results provide information about phase transformations as a function of weld time, but do not directly provide information about weld temperatures. In order to relate weld time to weld temperature, a numerical model was used, since transient weld temperatures are difficult to measure accurately. The weld model employed here is a well-tested 3-D numerical heat transfer and fluid flow model, which is described in detail in Ref. 16. The calculations are made in a fixed Cartesian coordinate system and take into account the electromagnetic, surface tension gradient, and buoyancy driving forces present in the transient weld pool convection (Ref. 16).

It should be noted that a common prac-

tice in the calculation of weld temperatures for linear welding is to use a constant arc efficiency to represent the amount of arc energy that transfers into the workpiece. This is a reasonable assumption, since the temperature field attains quasi-steady state soon after the start of welding. In contrast, for spot welding, temperatures change continuously and it takes several seconds for the arc to stabilize. In view of the lack of data on arc efficiency in the literature, a variable arc efficiency, which increases linearly from 0 to 75% in the first 3 s, is used to take into account the arc instabilities.

The thermo-physical properties used to represent the 1045 steel alloy in the calculations are given in Table 2 (Ref. 17). Since the 1045 steel contains 0.02 wt-% sulfur, the effect of sulfur on changing the surface tension is also included. In addition, at the weld top surface, the heat loss due to the helium shielding gas is considered by using Newton's law of cooling with an appropriate heat transfer coefficient, as described in a previous paper (Ref. 18).

For computational accuracy, the numerical model used a very fine grid system consisting of $108 \times 54 \times 59$ grid points, and the corresponding computational domain had dimensions of 140 mm long, 70 mm wide, and 50 mm deep. Spatially nonuniform grids were used for maximum resolution of the variables. Finer grids were used near the heat source where the temperature gradients are the highest. The minimum grid spacing along the x and z directions were about 20 µm and 5 µm, respectively. Small time steps of 0.01 s were further required to track the weld pool size and shape under the high heating and cooling rates produced under the transient welding conditions (Ref. 16).

The cross-sectional shape of the calculated weld pool at its maximum size matched the experimental weld cross sec-
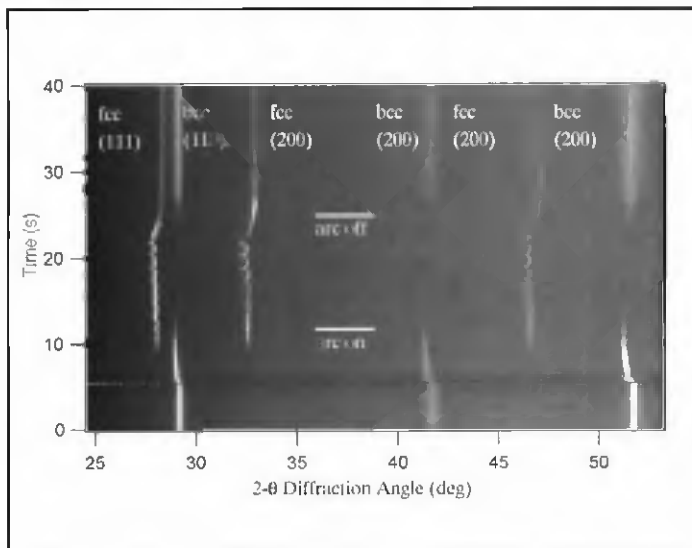
Fig. 4 — TRXRD results showing the changes in the diffraction peak locations as a function of welding time. Six peaks are present, three from each phase.
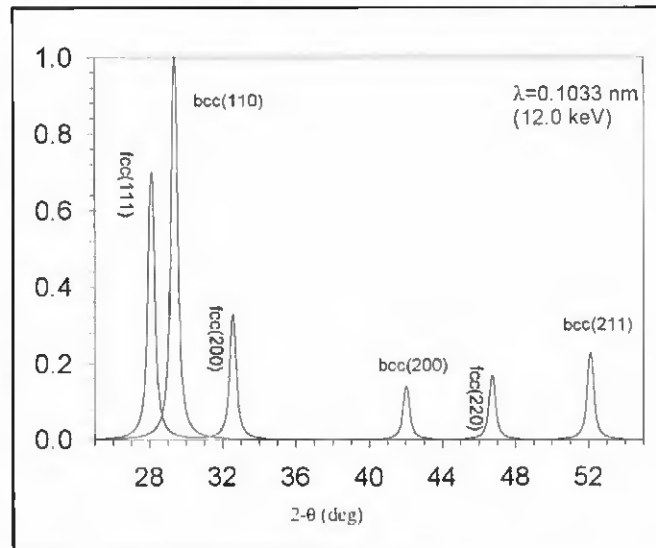

Fig. 5 — Calculated diffraction pattern, showing the six possible peaks in the detector window, assuming equal amounts of the FCC and BCC phases.

Table 2 — Summary of the Thermophysical Data for 1045 Steel Used in the Coupled Thermal Fluids Model to Predict Weld Temperatures

Liquidus temperature, T_L	1768 K
Solidus temperature, T_S	1713 K
Density of liquid metal, ρ	7.7×10^3 kg/m³
Effective viscosity of liquid, μ	0.16 kg/m·s
Effective thermal conductivity of liquid, k_L	335 W/m·K
Thermal conductivity of solid, k_S	36.4 W/m·K
Specific heat of solid, C_{PS}	586 J/kg·K
Specific heat of liquid, C_{PL}	746 J/kg·K
Temperature coefficient of surface tension, $d\gamma/dT$	-4.3×10^{-4} N/m·K
Coefficient of thermal expansion	1.51×10^{-5} K⁻¹
Convective heat transfer coefficient top surface	1.59×10^3 W/m²·K

Table 3 — Summary of JMA Modeling Results on 1045 Steel, and Comparison with Previous Data on 1005 Steel.

	Q (kJ/mole)	n	$\ln(k_0)$	E_{avg}
AISI 1045 steel with thermal cycle at $R = 4.75$ mm	117.1	0.95	11.4	0.049
AISI 1045 steel with thermal cycle at $R = 5.0$ mm	**117.1**	**0.82**	**12.2**	**0.052**
AISI 1045 steel with thermal cycle at $R = 5.25$ mm	117.1	0.60	13.4	0.075
AISI 1005 steel with thermal cycle at $R = 5.0$ mm	**117.1**	**1.45**	**12.3**	**0.099**

Note: The activation energy for the diffusion of carbon in austenite was held constant, and the JMA parameters n and $\ln(k_0)$ were calculated from TRXRD experimental data in all cases. The average error (E_{avg}) is defined as $(\sqrt{E_{fit}})/N$, and the bold-faced values correspond to the recommended parameters for the two steels.

tion having a width just under 10 mm and a maximum depth of 4.2 mm. Using the results from the weld model, the temperature distributions, heating rates, and cooling rates were calculated as a function of welding time at the TRXRD location.

These temperatures could then be coupled with the TRXRD results to develop time-temperature-transformation kinetic information about the transformations occurring during weld heating and cooling of the 1045 steel alloy.

Results

The TRXRD experiments were taken at a single location in the HAZ of the 1045 steel bar during welding. In situ diffraction patterns were recorded over a sufficient amount of time so that the entire heating and cooling cycle of the weld could be captured. These data are summarized in Fig. 4, where the diffraction patterns are displayed in a pseudo-color format. In this figure, the baseline diffraction data are shown for several seconds before the arc was turned on, for 17 s during the time when the arc was on, and for an additional 20 s of cooling time. Here, the higher peak intensities are indicated by the light tones, and lower peak intensities are indicated by dark tones, so that the diffraction peaks appear as streaks along the time axis at their appropriate 2θ locations over the range of times. Six diffraction peaks appear in Fig. 4. From low to high 2θ values, these peaks correspond to the FCC(111), BCC(110), FCC(200), BCC(200), FCC(220), and BCC(211), as indicated by the calculated diffraction pattern shown in Fig. 5.

Only three peaks corresponding to the BCC phase are present before the arc is initiated. After the arc is turned on, these three peaks rapidly shift to lower 2θ values due to the lattice expansion effect caused by weld heating. With continued heating, three new peaks, corresponding to the FCC phase, appear. All six peaks coexisted for several seconds before the BCC peaks began to fade in intensity, leaving only the FCC diffraction peaks. The FCC peaks are then stable until the arc is extinguished at $t = 17$ s, after which the FCC peaks rapidly shift to higher 2θ values due
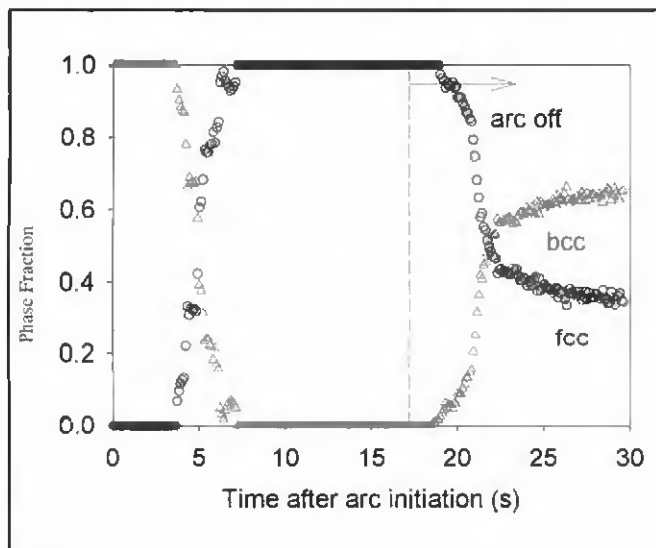
Fig. 6 — TRXRD measurements of the relative fraction of the BCC and FCC phases as a function of welding time.
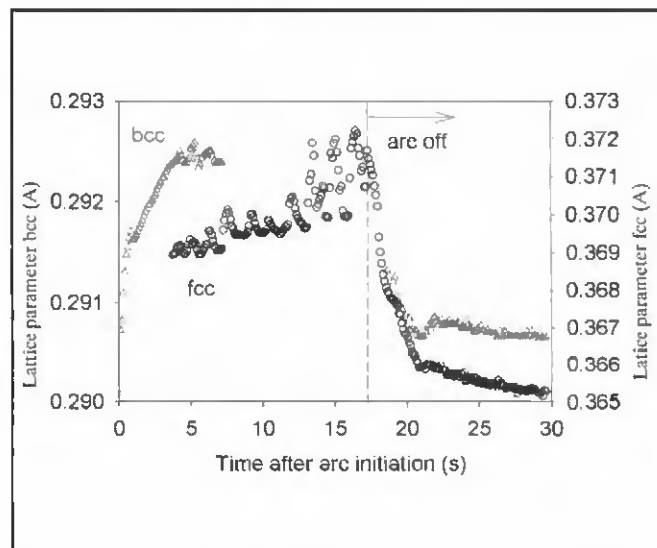

Fig. 7 — TRXRD measurements of the lattice parameter of the BCC and FCC phases as a function of welding time.

to the lattice contraction effect as the weld cools. After an additional 1.5 s of cooling time, the BCC peaks reappear and increase in intensity as the weld cools.

In Fig. 4, there is a wealth of information about the phases that exist at all times during the welding cycle; for example, information about the lattice parameters of each phase and how they change with welding time, plus other information such as the width, intensity, and areas of each of the diffraction peaks during the welding cycle. These additional data can be determined through individual peak profile analysis, and based on a portion of these data, the volume fraction of each phase during welding can be semiquantitatively estimated to provide other clues about the phase transformations taking place during welding.

The most important data gathered from the peak profile analysis are the relative fractions of the BCC and FCC phases present throughout both the heating and cooling cycles. These data are plotted in Fig. 6, showing that the alloy investigated starts out fully ferritic, then at $t=3.6$ s, begins to transform to austenite. The transformation takes 3.6 s to go to completion under the increasing temperature of the welding arc. The austenite phase is stable until the arc is turned off at $t=17.0$ s, and then continues to be the only phase for an additional 1.5 s while the weld cools. The BCC phase then appears at $t=18.5$ s, and continues to increase in amount as the FCC→BCC transformation proceeds. At the end of the experiment, the transformation appears incomplete, leaving some untransformed FCC at this point during weld cooling.

The lattice parameters of each phase can be determined from the 2θ positions

of the diffraction peaks using Bragg's law and the energy of the X-ray beam (Ref. 19). The results are plotted in Fig. 7, showing the lattice parameters of the BCC and FCC phases as a function of welding time. The lattice parameter of the BCC phase at room temperature was measured to be 2.901 Å, and increases rapidly to 2.925 Å during the initial heating cycle of the weld. The austenite phase first appears at $t=3.4$ s, when the ferrite lattice parameter was measured to be 2.923 Å. The lattice parameter of the FCC phase increases with welding time until the arc was turned off, then decreases rapidly during weld cooling. The BCC phase reappears during weld cooling at $t=18.5$ s where it has a lattice parameter of 2.914 Å. The lattice parameter of the BCC phase then decreases until $t=20.8$ s where it unexpectedly increases from 2.906 Å to 2.908 Å before continuing to decrease again as the weld continues to cool.

The widths of the diffraction peaks are plotted in Fig. 8 for the BCC(110) and FCC(111) phases. Both phases show similar trends during welding, whereby the peak widths decrease during heating and increase during cooling. The results show that the width of the BCC 110 peak is 0.14 deg in the starting condition and decreases to 0.04 deg just before it disappears at $t=7.2$ s. When the austenite peaks first appear, at $t=3.4$ s, the peak widths are about twice as wide as they are just before the arc is extinguished. The decrease in peak width with increasing temperature is caused by annealing, which creates more perfect diffraction conditions at higher temperatures. These phenomena have been observed in similar TRXRD experiments on other materials systems (Refs.

11, 14). Once the arc is extinguished, the rapid weld cooling causes the widths of the peaks to increase. The results show that the BCC peak widths increase more during cooling than they decreased during heating, suggesting that the rapid weld cooling has led to the creation of a different BCC phase after welding than before.

Discussion

α→γ Phase Transformation on Heating

The TRXRD results presented above provide information about the relative fractions of the BCC and FCC phases, their lattice parameters, and the widths of their diffraction peaks as a function of weld heating and cooling time. Included in these results is information related to the kinetics and types of phase transformations occurring in the HAZ during welding. Modeling of the experimentally measured transformation rates will be used to better understand the mechanisms behind each transformation and to develop parameters useful in the prediction of phase transformations.

It is known that the transformation of the pearlitic microstructure (ferrite and cementite) to austenite during heating is controlled by carbon diffusion in austenite (Ref. 20). In the experiments performed here, transformation of the microstructure during heating was shown to occur rapidly due to the high heating rate of the weld. Assuming the transformation is controlled by the diffusion of carbon in austenite, the kinetics of this transformation can be modeled by the Johnson-Mehl-Avrami (JMA) method (Refs. 4, 21). This approach has been used in a sim-
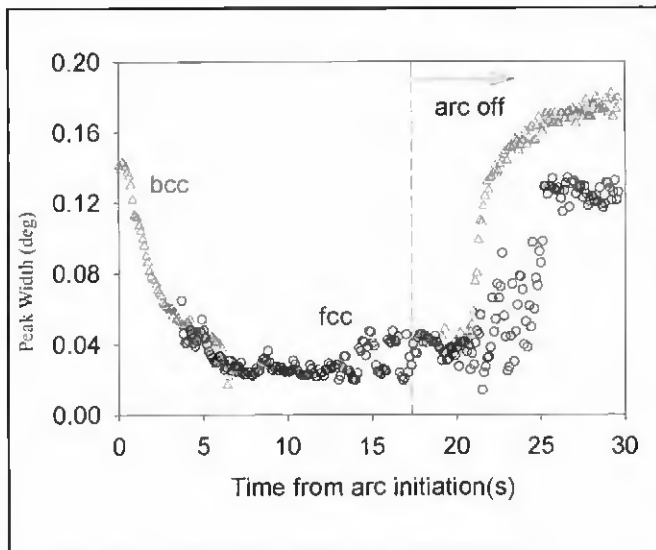
Fig. 8 — TRXRD measurements of the diffraction peak width of the BCC and FCC phases as a function of welding time.
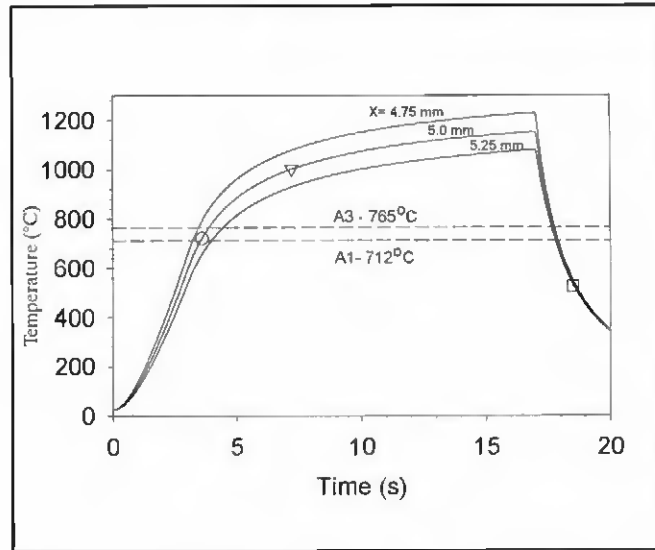

Fig. 9 — Calculated weld temperature at the X-ray beam location, 5.0 mm, and two adjacent locations. The open circle and triangle represent the times where the TRXRD measurements observed the start and finish of the transformation to austenite on heating, while the open square represents the first observation of the BCC phase on cooling.

ilar set of experiments on a typical low-carbon AISI 1005 C-Mn steel (Ref. 8). Using the available data, a set of parameters can be developed for use in predicting the extent of the phase transformation at different weld heating rates.

The JMA approach is represented by the following expression (Ref. 21):

$$f_e(t) = 1 - \exp\{-(kt)^n\} \tag{1}$$

where $f_e(t)$ is the extent of the transformation at a given time t, n is the JMA exponent, and k is a rate constant given as

$$k = k_0 \exp\left(-\frac{Q}{RT}\right) \tag{2}$$

where k_0 is a pre-exponential constant, Q is the activation energy of the transformation which includes the driving forces for both nucleation and growth, R is the gas constant, and T is the absolute temperature. By knowing the time-temperature profile of the weld, the three JMA parameters can be used to calculate the transformation rate.

Although the activation energy of phase transformations occurring under isothermal conditions is often known, the overall activation energy under nonisothermal welding conditions, in which nucleation and growth are operating simultaneously, is rarely known. The addition of the nucleation stage complicates the calculations because nucleation is both temperature and rate dependent and is influenced by the starting microstructure (Refs. 4, 21). Thus, a unique activation energy for the overall transformation is not always possible to determine. However, if a given transformation has a large growth component, it may be treated as a growth-controlled mechanism, and the activation energy for growth provides a reasonable starting assumption.

The results of the thermal model are shown in Fig. 9, which plots the calculated weld temperature vs. weld time at locations 4.75, 5.0, and 5.5 mm from the weld center. The 5.0 mm location is in the weld HAZ and corresponds to the position of the X-ray beam during the TRXRD experiment. Superimposed on this plot are the A1 and A3 temperatures and three symbols. The open circle and triangle represent the times when the start and finish of the transformation to austenite on heating, respectively, are observed. The open square represents the first observation of BCC phase on cooling. It is clear that superheating above the A3 temperature is required to complete the $\alpha \rightarrow \gamma$ transformation on heating, and that significant undercooling is required below the A1 temperature to initiate the $\alpha \rightarrow \gamma$ transformation.

Using the calculated time-temperature profile of the weld, Equations 1 and 2 were discretized and numerically integrated over the heating portion of the weld. This procedure was previously developed to calculate the degree of transformation in the two-phase field between the A1 and A3 temperatures of a 1005 C-Mn steel (Ref. 8). In these calculations, the TRXRD data were fit using the JMA parameters (n, k_0, and Q), by selecting one of the JMA parameters and calculating the remaining two using a numerical optimization routine (Ref. 8). The equilibrium start and completion temperatures for the $\alpha \rightarrow \gamma$ transformation used in the calculation are 712° and 765°C, respectively, as determined by *ThermoCalc*®. The equilibrium fraction of γ in the $\alpha + \gamma$ two-phase region was determined from the phase diagram as a function of temperature.

The best-fit JMA parameters were then calculated from the TRXRD experimental data. An activation energy for the diffusion of carbon in austenite was assumed to represent the $\alpha \rightarrow \gamma$ transformation. With a value of $Q=117.1$ kJ/mole (Ref. 8), a numerical fitting routine was used to determine the minimum error between the JMA fitting calculations and the experimentally determined austenite fraction as a function of $\ln(k_0)$ and n. The error (E_{fit}) between the two is defined by Equation 3:

$$E_{fit} = \sum_{i=1}^{N} \left(f_i^m - f_i^c\right)^2 \tag{3}$$

where N is the total number of measured data points, and f_i^m and f_i^c are the measured and calculated γ fractions at the ith data point, respectively. A total of 37 TRXRD data points were used in the calculation, and the optimization results are plotted in Fig. 10, showing that the optimal JMA values are $n = 0.82$ and $\ln(k_0) = 12.3$. Figure 11 compares the calculated and measured fractions of austenite as a function of time. The correlation is excel-
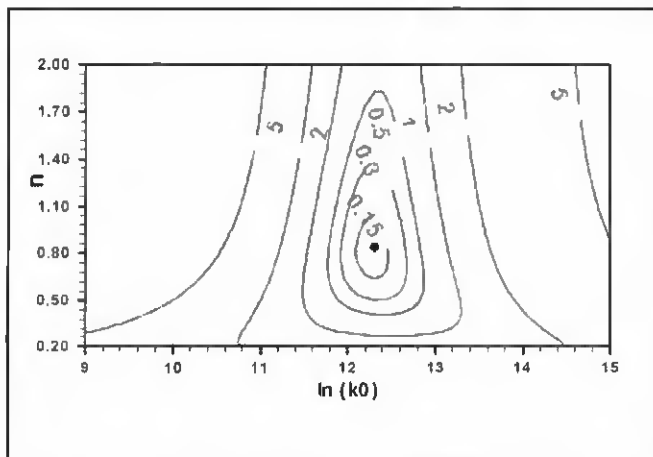
Fig. 10 — Error (E_{fit}) contour plot showing the optimal n and ln(k_0) values for the 1045 steel TRXRD data at the X=5.0 mm location. An activation energy of Q=117.1 kJ/mole was assumed, and the solid circle represents the optimal values of the JMA parameters n=0.82 and ln(k_0) = 12.3.
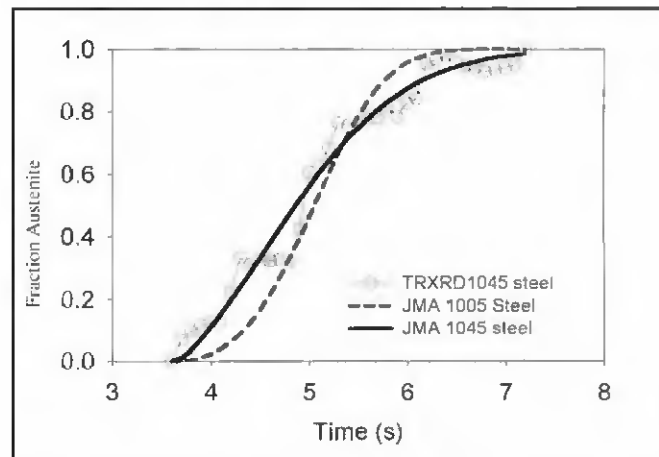

Fig. 11 — Kinetics of the ferrite to austenite transformation on weld heating. The TRXRD data for the 1045 steels are given by the circles and solid best-fit line are compared to the JMA parameters for 1005 steel (dashed line) from a previous study.

lent, showing that the JMA best fit to the experimental results adequately represents the data throughout the entire transformation range.

It should be noted that the above JMA kinetic parameters were calculated using the computed temperature vs. time data at X = 5.0 mm. There is good agreement between the TRXRD observations of the first formation of austenite and the calculated A1 temperature at this location. Although the distance from a monitoring location to the weld center is exact in the numerical calculation, there are certain errors in the spatial accuracy of the experimental TRXRD data. For the present TRXRD experiments, the uncertainty in the monitoring location of the beam is about ±0.25 mm. As shown in Fig. 11, the calculated temperatures for this uncertainty of ±0.25 mm in the monitoring location results in an uncertainty of ±70 K in the computed temperatures. This in turn contributes to uncertainties in the transformation kinetics.

To determine how much the temperature uncertainties affect the kinetic results, the optimization procedure described previously was used to calculate the JMA kinetic parameters for each of the three thermal cycles shown in Fig. 9. Table 3 summarizes these results, showing that the correlation for all three thermal cycles is reasonable. Due to the uncertainty in the monitoring location, the uncertainties in the values of n and ln(k_0) were calculated to be about ±0.2 and ±1.0, respectively. Due to the lack of kinetic data in the literature, the calculated JMA kinetic parameters cannot be further verified, and the lack of available data emphasizes the need for additional quantitative investigations on this topic.

A similar set of JMA parameters was developed in an earlier study for 1005 (0.05 wt-% C) (Ref. 8). The JMA kinetic parameters determined for this steel were $n = 1.45$ and ln(k_0) = 12.2, for an assumed activation energy (Q) of 117.1 kJ/mole. The JMA parameters determined for the 1005 steel were then used to compare transformation rates between 1005 steel and 1045 steel. To do this, the JMA parameters for the 1005 steel were used to predict the fraction austenite for the same time-temperature profile calculated for the 1045 steel weld in this investigation. The results are superimposed on the 1045 steel results in Fig. 11, where the dashed line represents the predicted transformation for 1005 steel, and the solid line for the 1045 steel. Even though the two curves start and finish at approximately the same times, there are some differences. For example, the transformation rate of the 1045 steel is initially somewhat higher than that of the 1005 steel, but slows down to values less than that of the 1005 steel. At approximately 5.5 s after the arc was initiated, the total fraction transformed in each steel is approximately the same (0.75). The higher transformation rate of the 1005 steel at this point allows it to complete the transformation to austenite approximately 1 s sooner than that of the 1045 steel.

There are several possible reasons for the differences in the transformation rates for the two steels. First, the different carbon contents of the two steels resulted in different starting microstructures. The principal microstructural difference is the amount of pearlite in each. In the 1005 steel, which contained less than 10% pearlite, small pearlite colonies were isolated along the ferrite grain boundaries. In the 1045 steel, which contained 88% pearlite, the pearlite occupied the majority of the microstructure, leaving a rela-

tively small amount of allotriomorphic ferrite at the prior austenite grain boundaries. The second microstructural difference between the two steels was the starting grain size. Both steels contained equiaxed grains; however, the grain size of the 1045 steel was 92.8 µm, which is more than four times larger than that of the 1005 steel, which had a base metal grain size of only 21.5 µm.

The differences in starting grain size and amount of pearlite between the 1005 and 1045 steels lead to different transformation rates between the two steels. Since the austenite nucleation rate is higher in pearlite than in ferrite, due to its fine dispersion of cementite in the lamellar pearlitic structure, one would expect that the 1045 steel, which has the higher fraction of pearlite, would transform to austenite more quickly than the 1005 steel. However, the 1045 steel transforms more rapidly only during the early stages of the transformation, up to an austenite fraction of approximately 0.75. Thus, other factors are coming in to play that reduce the overall transformation rate of the 1045 steel relative to that of the 1005 steel as the transformation continues.

The other significant difference between the two steels was the starting grain size, which is four times larger for the 1045 steel than for the 1005 steel. It is known that the transformation rate of diffusion-controlled reactions will decrease as the grain size gets larger (Refs. 4, 21) because diffusion is required to take place over larger distances to complete the transformation in the larger grain sized materials. In the 1045 steel, the large amount of pearlite helps to offset the grain size difference by providing numerous nucleation sites within the pearlite. However, the large grain size of the allotriomorphic fer-
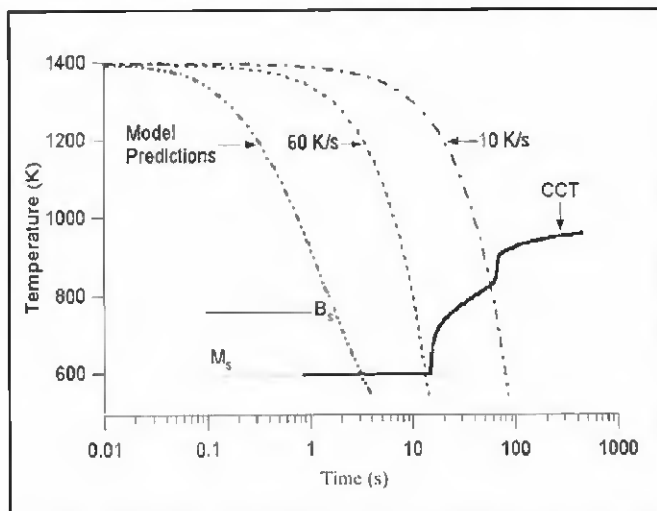
Fig. 12 — Calculated continuous cooling transformation diagram for the AISI 1045 steel. The three curves correspond to the minimum cooling rate needed to avoid pearlite formation (10°C/s), the maximum rate needed to avoid martensite formation (60°C/s), and the cooling rate for the TRXRD weld.
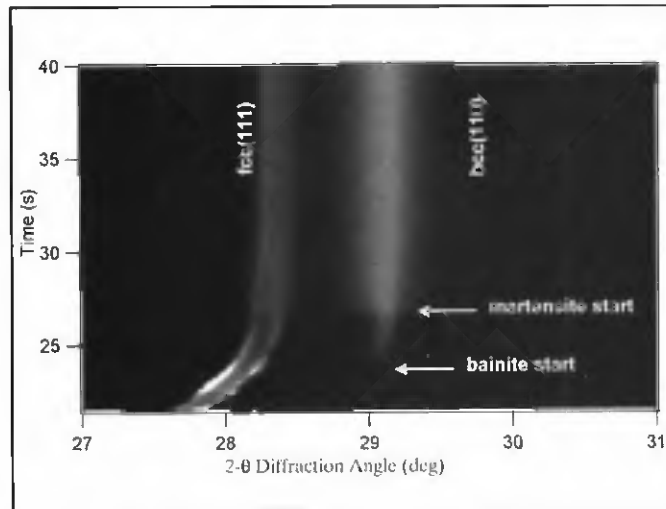

Fig. 13 — TRXRD results showing the FCC(111) and BCC(110) diffraction peaks during weld cooling. The martensite transformation results in a rapid increase in diffraction peak width for the BCC phase.

rite regions in the 1045 steel has an indirect effect on the transformation rate. These large ferrite regions should be the last portion of the 1045 steel microstructure to transform and, as such, will control the total amount of time required to completely austenitize the microstructure. Since the allotriomorphic patches in the 1045 steel exceeded 30 μm in places, one might expect that the total time required to transform the 1045 steel would be longer than that of the 1005 steel, which had an average grain size of 21.5 μm.

Therefore, the JMA kinetic analysis of the TRXRD data adequately describes the α→γ transformation kinetics of the 1045 steel, providing a quantitative means for predicting austenite formation in the HAZ of similar carbon content steel welds. Comparisons between the α→γ transformation kinetics of the 1045 steel and 1005 steel illustrated how the carbon content affects the transformation rate through its effect on the starting microstructure of the base metal. Additional work is planned to look at even higher-carbon steel welds in order to further extend these observations.

γ→α Phase Transformation on Cooling

The cooling transformations in steel can be more complicated than the heating transformations because of the potential formation of nonequilibrium phases at high cooling rates. It is already known that diffusion-dependent transformations, such as the formation of pearlite, a lamellar microstructure of alternating ferrite and cementite phases, occur at low cooling rates (Ref. 3). As the cooling rate increases, diffusion of carbon may not be rapid enough to allow the lamellar pearlite

microstructure to form. Shear-type transformations thus begin to dominate at these higher cooling rates. For example, bainite, which is characterized by a microstructure of mixed ferrite and cementite with non-lameller features, forms through a combination of diffusion and shear at intermediate cooling rates (Ref. 3). Martensite, on the other hand, forms entirely by a shear mechanism and only at high cooling rates, producing a microstructure containing lath or plate-like characteristics with the carbon trapped in interstitial sites of the crystal lattice (Ref. 3).

The formation of bainite and martensite cannot be described by the equilibrium phase diagram presented in Fig. 2, since these transformations occur under nonequilibrium conditions. However, one can use calculated continuous cooling transformation (CCT) diagrams to provide information about microstructural evolution during continuous cooling. In this work, we used the model developed by Bhadeshia et al. (Refs. 22, 23), to predict the continuous cooling transformation diagram for the AISI 1045 steel — Fig. 12. The diagram was constructed from time-temperature-transformation (TTT) data calculated from paraequilibrium thermodynamics of the α→γ transformation by using the additivity rule (Ref. 24), and predicts the onset of the different transformations that can occur during cooling. The CCT diagram was overlaid with three different cooling curves, one predicted by the heat transfer and numerical model from Fig. 9 and two other linear cooling rates of 10°C/s and 60°C/s from a peak temperature of 1124°C. The plots show that a minimum cooling rate of 10°C/s is needed to avoid the formation of ferrite + pearlite microstructure. Moreover, a max-

imum cooling rate of 60°C/s is needed to avoid the formation of martensite. The bainite start temperature for this steel is predicted to be 485°C, and martensite start temperature is predicted to be 324°C. Both temperatures are far below the equilibrium A1 temperature. The predicted cooling rate by the heat transfer model is higher than 60°C/s and therefore a predominantly martensitic microstructure is expected in the final microstructure.

Figure 13 shows the results of TRXRD experiments on cooling for the FCC(111) and the BCC(110) diffraction peaks. As soon as the arc is extinguished, the FCC(111) peak rapidly shifts to higher 2θ values due to the lattice contraction effect. At $t = 18.6$ s, the BCC(110) peak first appears and has a relatively narrow peak width. This peak shifts to higher 2θ as the weld continues to cool and increases in intensity. At $t = 20.8$ s, both the BCC(110) and the FCC(111) peaks show a sudden increase in width. The wider BCC(110) peak exists throughout the remainder of the weld, increasing in intensity as the weld continues to cool, and shifting to slightly higher 2θ values.

The sudden increase in the BCC(110) peak width at low temperatures was not observed in similar experiments performed on a low-carbon AISI 1005 steel (Refs. 7–9). The increase in peak width is caused by strain in the lattice, i.e., the opposite of the annealing effect, and/or changes in the composition or crystal structure. The formation of martensite would explain the rapid broadening of the diffraction peaks, since its formation would trap carbon in the BCC lattice. This would both strain the lattice and create changes in the lattice parameter through the formation of a body-centered tetragonal (BCT) crystal structure. The
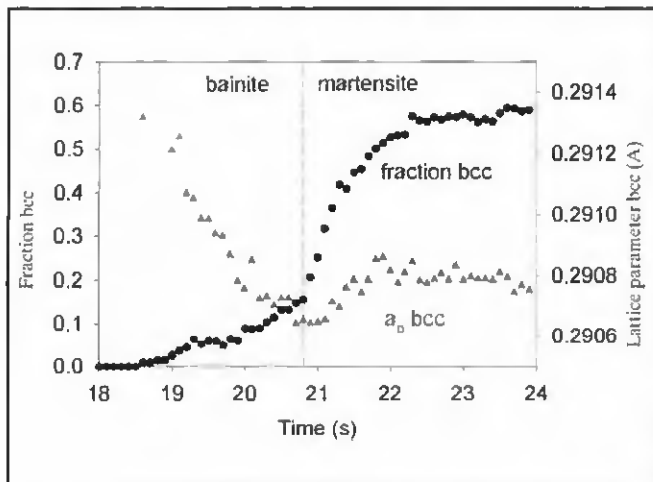
Fig. 14 — Fraction and lattice parameter of the BCC phase as a function of weld cooling time. The transition from bainite to martensite occurs at t=20.8 s, showing an increase in transformation rate and an increase in the BCC lattice parameter.
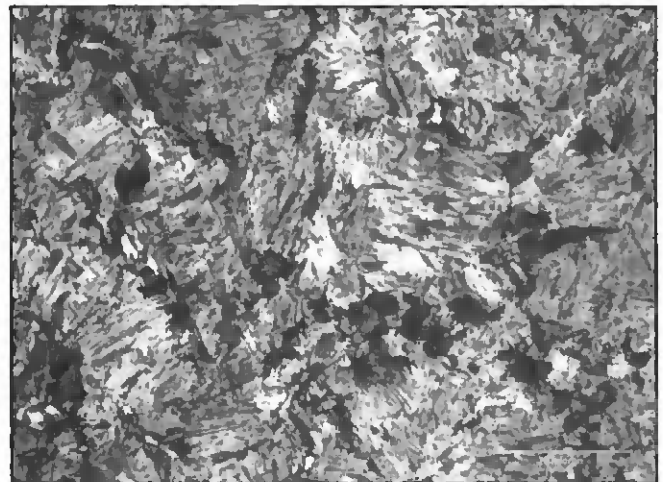

Fig. 15 — Photomicrograph in the HAZ at the location where the TRXRD data were taken, showing a bainitic/martensitic postweld microstructure.

strain induced by the martensite would also explain similar changes in the broadening of the austenite peaks that occurred at the same time.

In order to determine if the martensitic transformation is responsible for the peak broadening, the area fractions of the FCC(111) and BCC(110) peaks were measured from the TRXRD data to determine the transformation rate during weld cooling. These results are plotted vs. weld time during cooling in Fig. 14. The fraction of the BCC phases is given by the solid circles in this plot, which shows that the first BCC phase appears at t=18. The initial rate of increase in the BCC phase is relatively slow, reaching approximately 15% transformed at t=20.8 s. At this time, the BCC peaks rapidly increase in width, leading to a corresponding increase in the transformation rate. This increase in rate is more than two times higher than that measured up to this point, indicating that there is a change in the transformation mechanism. Such an increase in the transformation rate would not be expected at lower temperatures during weld cooling unless a different kinetic path is taken. The transformation continues as the temperature decreases, achieving approximately 60% transformed at t=24 s.

A martensitic transformation would explain the change in transformation mechanism at these low temperatures, whereby the $\gamma \rightarrow \alpha$ transformation initiated by a bainitic mechanism and switched to a martensitic mechanism at low temperatures. It is important to note that the CCT diagram of Fig. 12 did not predict the initial formation of bainite. However, bainite formation is possible if there was a nonuniform distribution of carbon in the austenite prior to the transformation. This nonuniform distribution of carbon would

he possible if the weld HAZ were not completely homogenized during the rapid weld heating and cooling cycle.

Further indications of the martensitic portion of the cooling transformation are provided by changes in the peak widths and lattice parameters. The widening of the peaks, as described above, is consistent with a martensitic transformation, due to its stressed lattice and BCT crystal structure (Ref. 3). In addition, an increase in the lattice parameter of the BCC phase would be consistent with the formation of BCT martensite. Figure 14 also plots the measured lattice parameter as a function of welding time, and combines these data with the fraction of the BCC phase. A decrease in the lattice parameter for the BCC phase is observed during the initial stages of transformation leading up to the change in mechanism at t=20.8 s. This behavior would be expected if the initial stage of transformation were occurring by either the formation of bainite, since its lattice parameter would decrease as the weld cools. At t=20.8 s, when the transformation rate increases, there is an increase in the lattice parameter from 2.906 to 2.908 Å. This increase in lattice parameter is qualitatively consistent with the formation of martensite and provides further evidence that the transformation initiating at t=20.8 s is martensitic.

The temperatures at which these transformations occur also give indications about the mechanisms governing the observed transformations. Figure 9 shows that the first BCC phase appeared at t=18 s, and that martensite initiated at t=20.8 s. Using the calculated temperature profile, the martensite initiated at a temperature of 280°C. This temperature is well below the A1 temperature, and is slightly lower than the martensite start temperature of

323°C predicted by the CCT diagram. Thus, this temperature is qualitatively consistent with the formation of martensite.

The temperature where the first BCC phase appeared on cooling at t=18 s was calculated to he 526°C, which is also well below the A1 temperature of this steel. At this temperature, the cooling rate of the weld was calculated to he 178°C/s, which is fast enough to avoid the formation of pearlite. The calculated CCT diagram shown in Fig. 12 indicates that the nose of the bainite initiation curve occurs at approximately 550°C, which matches well with the TRXRD results of 526°C, and provides further evidence that the transformation from austenite to ferrite is initiated by a bainitic mechanism.

Microstructural observations of the weld HAZ indicate that the final microstructure does indeed contain a mixture of bainite and martensite phases. Figure 15 shows the microstructure of the HAZ at the location where the TRXRD data were obtained. In this microstructure, the prior austenite grain boundaries in the weld HAZ are much smaller than those in the original hase metal as a result of the numerous nucleation sites provided within the original pearlite microstructure. No pearlite is present, and grain boundary ferrite is minimal. The hainitic portions of the microstructure appear as the darker etching patches of the microstructure localized at the prior austenite grain boundaries. Within the grains, the microstructure is highly refined, and is characteristic of lath martensite that forms during rapid cooling of medium-carbon steels (Ref. 3). Therefore, the TRXRD results were able to distinguish between martensite and bainite phases based on their transformation rates, lattice parameters, and temperatures where they initiated. Additional experiments are planned on higher-carbon

steels where the amount of martensite formed will be greater, and where the effects of carbon on the microstructure will be even more apparent.

Conclusions

TRXRD experiments were performed in the HAZ of AISI 1045 steel during stationary arc welding. These experimental observations provided real-time in situ diffraction patterns of the phase transformations occurring during rapid weld heating and cooling.

Diffraction peak profile analysis was used to determine the relative fraction of BCC and FCC phases during the welding cycle, as well as the lattice parameters and diffraction peak widths for each of the phases during the entire weld cycle.

A 3-D transient numerical weld model was used to predict weld temperatures as a function of weld time and location. The model calculated the evolution of the FZ velocity fields and temperatures, and was validated by comparing the predicted and experimentally measured geometry of the FZ.

The TRXRD results and the weld temperatures were used to model the kinetics of the $\alpha \rightarrow \gamma$ phase transformation during weld heating of the 1045 steel using a Johnson-Mehl Avrami analysis. The results yielded kinetic parameters for the JMA prediction of the transformation of $n = 0.82$ and $\ln(k_0) = 12.3$ for an activation energy of $Q = 117.1$ kJ/mole.

The JMA results of the $\alpha \rightarrow \gamma$ phase transformation of the 1045 steel measured here were compared with previously calculated JMA parameters for a low-carbon 1005 steel. Differences between the two steels showed that the initial transformation rate of the 1045 steel is more rapid than that of 1005 steel, but that the transformation rate of the 1045 steel slows down, eventually requiring more time than the 1005 steel to complete the transformation to austenite.

The transformation rates of both steels appear to be controlled by the diffusion of carbon, and were influenced by the relative fraction of pearlite in the starting microstructure and the starting grain size of the steel. The higher fraction of pearlite in the microstructure of the 1045 steel resulted in its initial high transformation rate, but its larger grain size, combined with its large patches of allotriomorphic ferrite, resulted in its longer total transformation time.

During rapid weld cooling, the austenite that formed in the HAZ of the 1045 steel was shown to back transform to ferrite with significant undercooling below the A1 temperature. This transformation initiated as a BCC phase with a relatively narrow diffraction peak width at 526°C, which was shown to be the result of a bai-

nite transformation mechanism.

During continued cooling, the transformation rate suddenly increased twofold, and the BCC diffraction peak width and lattice parameters increased dramatically at a temperature of 280°C. These effects were attributed to the formation of martensite, which completed the transformation.

These TRXRD experiments represent the first real-time diffraction observations of the formation of bainite and martensite during the welding of steels.

References

1. Honeycomb, R. W. K., and Bhadeshia, H. K. D. H. 1982. *Steels, Microstructure and Properties.* Metals Park, Ohio: ASM International.

2. Bhadeshia, H. K. D. H. 2001. *Bainite in Steels.* 2nd ed. Institute of Materials, London.

3. Krauss, G. 1980. *Steels: Principles of Heat Treating of Steels.* Metals Park, Ohio: ASM International.

4. Grong, Ø. 1994. *Metallurgical Modelling of Welding,* chap. 1. London, U.K.: The Institute of Materials.

5. Ashby, M. F., and Easterling, K. E. 1982. A first report on diagrams for grain growth in welds. *Acta Metall.* 30:1969.

6. Ion, J. C., Easterling, K. E., and Ashby, M. F. 1984. A second report on diagrams of microstructure and hardness for heat-affected zones in welds. *Acta Metall.* 32:1949.

7. Elmer, J. W., Wong, J., and Ressler, T. 2001. Spatially resolved X-ray diffraction mapping of phase transformations in the HAZ of carbon-manganese steel arc welds. *Metall. and Mater. Trans. A* 32A(5): 1175–1187.

8. Elmer, J. W., Palmer, T. A., Zhang, W., Wood, B., and DebRoy, T. 2003. Kinetic modeling of phase transformations occurring in the HAZ of C-Mn steel welds based on direct observations. *Acta Materialia* 51: 3333–3349.

9. Wong, J., Ressler, T., and Elmer, J. W. 2003. Dynamics of phase transformations and microstructure evolution in carbon-manganese steel arc welds using time resolved synchrotron X-ray diffraction. Part 2. *J. Synchrotron Radiation* 10(3): 154–167.

10. Elmer, J. W., Wong, J., and Ressler, T. 1998. Spatially resolved X-ray diffraction phase mapping and $\alpha \rightarrow \beta \rightarrow \alpha$ transformation kinetics in the HAZ of commercially pure titanium arc welds. *Metall. Mater. Trans. A* 29A(11): 2761.

11. Elmer, J. W., Palmer, T. A., and Wong, J. 2003. In-situ observations of phase transitions in Ti-6Al-4V alloy welds using spatially resolved X-ray diffraction. *Journal of Applied Physics* 93(4): 1941–1947.

12. Babu, S. S., Elmer, J. W., David, S. A., and Quintana, M. 2002. In-situ observations of non-equilibrium austenite formation during weld solidification of a Fe-C-Al-Mn low alloy steel. *Proceedings of the Royal Society: Mathematical, Physical and Engineering Sciences* 458: 811–821.

13. Elmer, J. W., Wong, J., and Ressler, T. 2000. In-situ observations of phase transformations during solidification and cooling of austenitic stainless steel welds using time-resolved X-ray diffraction. *Scripta Materialia* 43(8): 751–757.

14. Palmer, T. A., Elmer, J. W., and Wong, J. 2002. In-situ observations of ferrite/austenite transformations in duplex stainless steel weldments using synchrotron radiation. *Science and Technology of Welding and Joining* 7(3): 159–171.

15. Sundman, B., Jansson, B., and Andersson, J. 1985. *Calphad — Computer Coupling of Phase Diagrams and Thermochemistry* 9(2): 153.

16. Zhang, W., Roy, G. G., Elmer, J. W., and DebRoy, T. 2003. Modeling of heat transfer and fluid flow during GTA spot welding of 1005 steel. *Journal of Applied Physics* 93(5): 3022–3033.

17. Cverna, F. 2002. *Thermal Properties of Metals.* Materials Park, Ohio: ASM International.

18. Elmer, J. W., Palmer, T. A., Babu, S. S., Zhang, W., and DebRoy, T. 2004. Phase transformation dynamics during welding of Ti-6Al-4V. *Journal of Applied Physics* 95(12): 8327–8339.

19. Cullity, B. D., and Stock, S. R. 2001. *Elements of X-Ray Diffraction,* 3rd Ed. Upper Saddle River, N.J.: Prentice Hall.

20. Speich, G. R., Demarest, V. A., and Miller, R. L. 1981. Formation of austenite during intercritical annealing of dual phase steels. *Metallurgical Transactions A* 12A:1419.

21. Christian, J. W. 1975. *Theory of Transformations in Metals and Alloys,* Part I, 2nd Ed. Oxford, U.K.: Pergamon.

22. Bhadesia, H. K. D. H., Svensson, L. E., and Gretoft, B. 1985. A model for the development of microstructure in low-alloy steel (FE-MN-SI-C) weld deposits. *Acta Metallurgica* 33(7): 1271.

23. Bhadesia, H. K. D. H. 1982. Thermodynamic analysis of isothermal transformation diagrams. *Metal Science* 16(3): 159.

24. Babu, S. S., and Bhadesia, H. K. D. H. 1990. Transformation from bainite to acicular ferrite in reheated Fe-Cr-C weld deposits. *Materials Science and Technology* 6(10): 1005.